

A universal model for solar eruptions

Peter F. Wyper¹, Spiro K. Antiochos² & C. Richard DeVore²

Magnetically driven eruptions on the Sun, from stellar-scale coronal mass ejections¹ to small-scale coronal X-ray and extreme-ultraviolet jets^{2–4}, have frequently been observed to involve the ejection of the highly stressed magnetic flux of a filament^{5–9}. Theoretically, these two phenomena have been thought to arise through very different mechanisms: coronal mass ejections from an ideal (non-dissipative) process, whereby the energy release does not require a change in the magnetic topology, as in the kink or torus instability^{10,11}; and coronal jets from a resistive process^{2,12} involving magnetic reconnection. However, it was recently concluded from new observations that all coronal jets are driven by filament ejection, just like large mass ejections¹³. This suggests that the two phenomena have physically identical origin and hence that a single mechanism may be responsible, that is, either mass ejections arise from reconnection, or jets arise from an ideal instability. Here we report simulations of a coronal jet driven by filament ejection, whereby a region of highly sheared magnetic field near the solar surface becomes unstable and erupts. The results show that magnetic reconnection causes the energy release via ‘magnetic breakout’—a positive-feedback mechanism between filament ejection and reconnection. We conclude that if coronal mass ejections and jets are indeed of physically identical origin (although on different spatial scales) then magnetic reconnection (rather than an ideal process) must also underlie mass ejections, and that magnetic breakout is a universal model for solar eruptions.

To test quantitatively the hypothesis that coronal jets are in fact miniature versions of coronal mass ejections, we performed an ultrahigh-resolution three-dimensional simulation that captures as closely as possible the salient features of a coronal jet magnetic system containing a so-called “mini-filament”^{13,14}; this is a miniature version of the large-scale filaments that form in filament channels and erupt as coronal mass ejections. This high-resolution adaptive-mesh calculation clearly resolves the different stages of the mini-coronal mass ejection (CME) jet. The setup is similar to our previous calculations^{15,16} (see Methods). To represent an emerged bipolar region in a solar coronal hole, we start with a strong bipole embedded in an inclined, uniform, ambient field (Fig. 1a). This configuration naturally creates the loop field structure (sometimes called the anemone region)¹⁷ observed at the base of coronal jets, with a domed separatrix surface and three-dimensional null point at the boundary between the open- and closed-field regions. The initial system is current-free and therefore has no filament and no free energy with which to power an eruption. We energize the system and create the filament by shearing the footpoints of field lines connecting to the parasitic (positive) polarity over a finite time interval. The driving is subsonic and sub-Alfvénic so that the shear is built up quasi-statically, and the driving is localized to a narrow region about the polarity inversion line so that a filament-channel-like structure develops. This shearing is merely a numerically convenient way to inject free energy into the field near the polarity inversion line, where we know the energy must be stored owing to the positioning of the mini-filament. The driving could represent energy injection/storage at the polarity inversion line via very slow flux emergence or cancellation,

photospheric shearing motions, or helicity condensation¹⁸ (the cumulative effect of quasi-random surface motions). We end the slow footpoint shearing well before any evidence of jetting activity in our simulation. Consequently, the shearing serves only to provide free energy to the system; it does not directly drive the resulting explosion.

Figure 2a shows the strongly sheared magnetic field (yellow) created by the end of the driving period. Such a field structure is observed to support cool, dense plasma against gravity in large-scale filaments¹⁹ and is expected to exist within the mini-filaments involved in coronal jets. The overlying restraining field (magenta) pins the filament down near

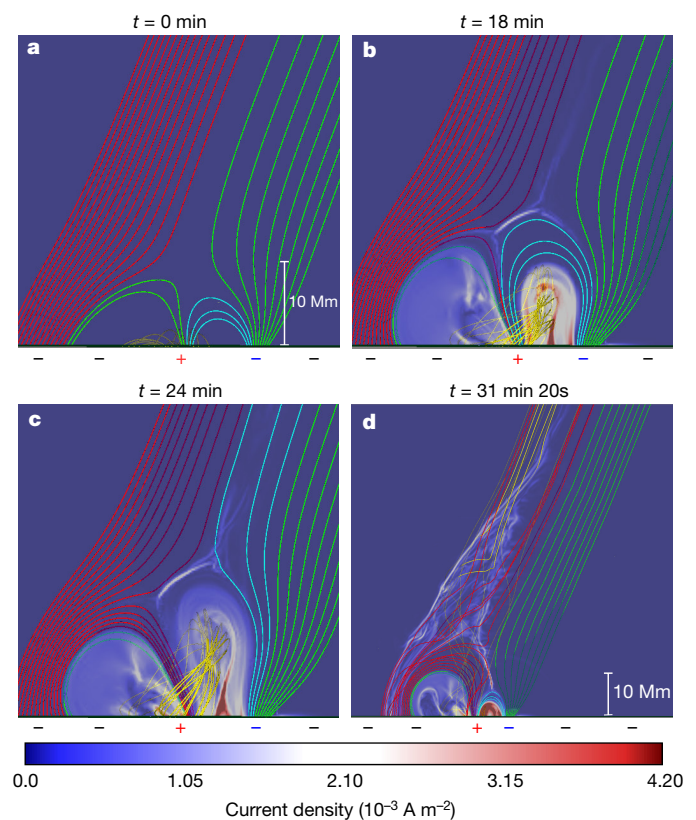


Figure 1 | The simulated mini-filament jet evolution. a–d, Red plus symbols and blue minus symbols indicate the bipole position; black minus symbols indicate the background field. Field lines are coloured to depict the various magnetic field regions (compare with Fig. 3): the filament or flux-rope structure (yellow; **b**, **c**) forms beneath the central arcade (blue; **a**, **b**), which reconnects with overlying field (red) to transfer flux into the side arcades (green), and subsequently erupts (**d**). Semi-transparent shading shows current density (colour scale) in the plane. The thin strip of high current density near the centre of the panel (**b**, **c**) depicts the breakout current sheet formed at the null point. The flare current sheet is short when it first forms below the slowly rising flux rope (**c**), but elongates vertically and strengthens substantially as the flux rope accelerates (**d**).

¹Department of Mathematical Sciences, Durham University, Durham DH1 3LE, UK. ²Heliophysics Science Division, NASA Goddard Space Flight Center, 8800 Greenbelt Road, Greenbelt, Maryland 20771, USA.

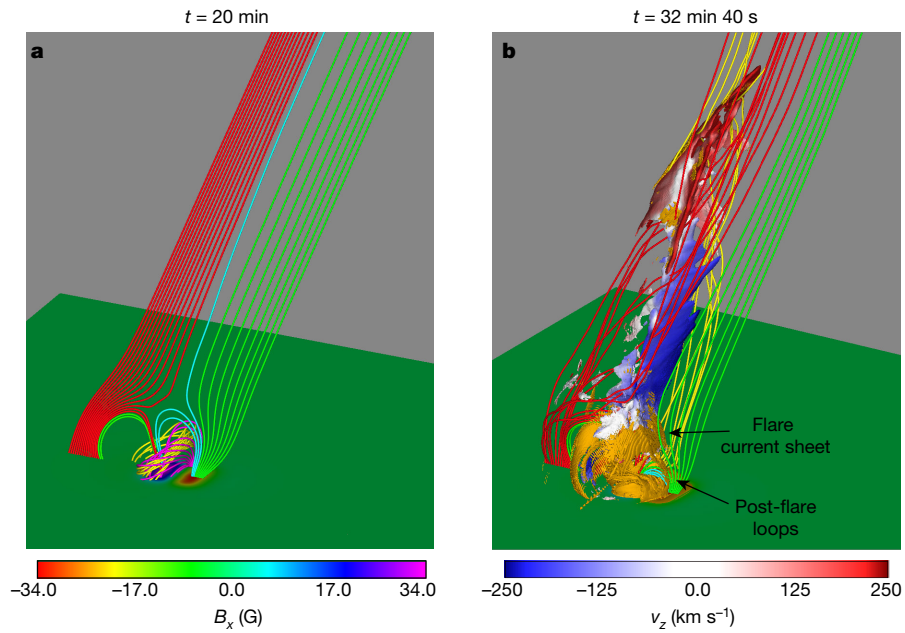


Figure 2 | Three-dimensional structure of the filament field and the jet. **a, b**, The photosphere (bottom plane, principally dark green) is shaded according to the vertical magnetic field B_x (colour scale in **a**).

Isosurfaces show current density ($|J| = 1.8 \times 10^{-3} \text{ A m}^{-2}$; orange) and velocity magnitude ($|v| = 250 \text{ km s}^{-1}$; red/blue colour shading denotes the untwisting horizontal component, v_z , on this isosurface; colour scale in **b**).

the photosphere (dark green). Whether the filament will erupt depends on whether it can overcome this restraining field.

The breakout model for large-scale CMEs^{20,21} offers a natural avenue for this to occur. It asserts that when magnetic shear is added at the polarity inversion line of an arcade beneath a coronal null point (Fig. 3a, b), the overlying restraining field must expand upward and create a current sheet at the null point. Reconnection at this sheet then slowly removes the restraining field. Beyond a critical threshold, a feedback (breakout) process is initiated whereby the removal of the restraining field leads to a runaway upward expansion of the sheared field²⁰. This expansion stretches the sheared field to the point that another current sheet with further magnetic reconnection is initiated beneath the erupting field (Fig. 3c, d), forming and expelling the CME flux rope and generating the intense flare loops²¹.

We find a similar evolution in our ‘breakout jet’ configuration (see Fig. 1 and also Supplementary Video 1). As the strongly sheared field

builds up along the polarity inversion line between the flux concentrations of the bipole, the restraining field (blue) expands upwards towards the null point (Fig. 1b). This creates the breakout current sheet that reconnects the restraining field to the closed field on the other side of the null point and to the open field (Fig. 1b, c). Thus, the breakout reconnection removes the restraining field and also produces a slow, tapered outflow of plasma. As the filament field continues to expand, slow internal reconnection turns the sheared-field region into a twisted flux rope, the structure required for kink or torus instability^{10,11}. Continued breakout reconnection slowly lifts the flux rope towards the breakout current sheet. The rise speed of the flux rope increases from around 10 km s^{-1} to 40 km s^{-1} during this phase (Extended Data Fig. 1), agreeing with the observed values and explaining the slow-rise phase of mini-filaments in coronal jets¹³ (Fig. 1b, c). The key result is that little energy is released during this time, as expected for the breakout process²¹ (Fig. 4). Explosive energy release occurs only when the flux rope reaches the breakout sheet and reconnects onto the open field.

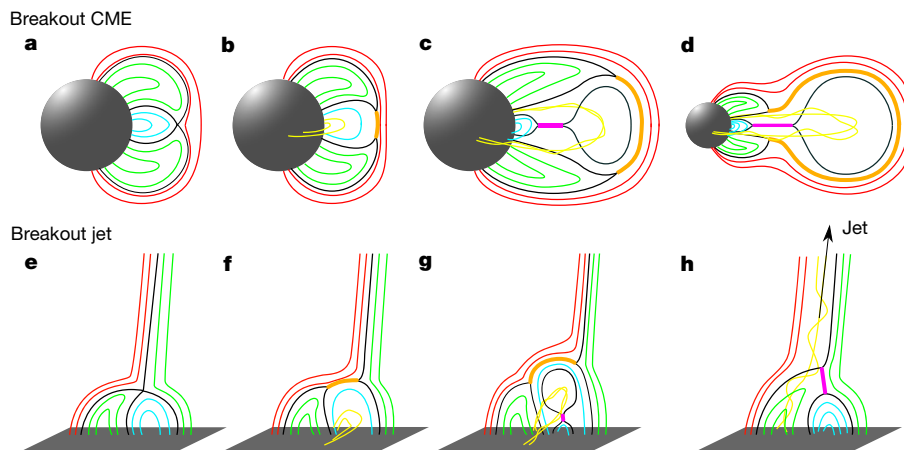


Figure 3 | Schematic of the breakout process. **a–d**, In CMEs; **e–h**, in jets. Time increases from left to right. The grey sphere (**a–d**) is the entire solar surface; the grey sheet (**e–h**) is a local patch of the surface. Black field lines show separatrices (or quasi-separatrices) dividing different regions of the

magnetic field (red, green, blue). Yellow field lines show the core of the filament (or flux rope). The thick orange line denotes the breakout current sheet, and the thick pink line the flare current sheet.

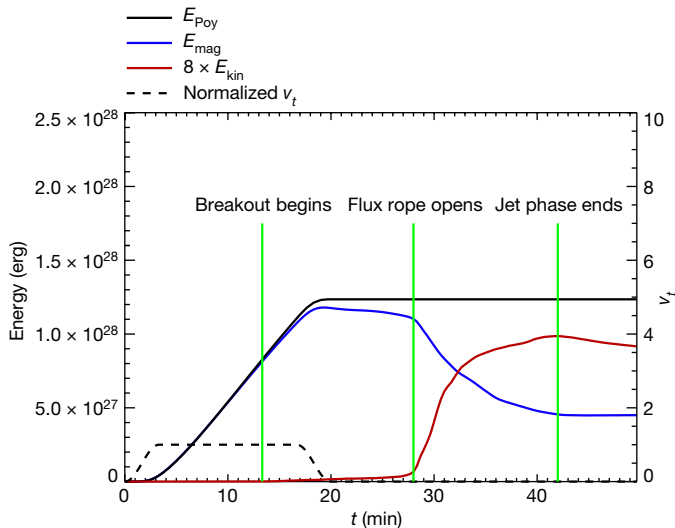


Figure 4 | Energy stored and released during the simulation. Magnetic energy injected as cumulative Poynting flux, E_{Poy} (black solid line); free magnetic energy stored in the volume, E_{mag} (blue line); and kinetic energy of plasma motion, E_{kin} (red line). The time profile of the driver normalized by the maximum driving speed (black dashed line) and key transition times in the simulation (green lines) are also shown.

In our simulation, the eruption is clearly due to a resistive process—reconnection—not to an ideal process.

The rapid reconnection between the twisted flux rope and the background open field launches an untwisting jet along the ambient open field, while simultaneously stretching the sheared field to initiate flare reconnection and form the flare loops (Fig. 1d). The jet itself is a combination of a nonlinear torsional Alfvén wave and the Alfvénic outflow emanating from the flare current sheet. The torsional wave component is launched when the twist within the flux rope begins to spread along the ambient open field, following reconnection at the breakout current sheet. Magnetic tension around the periphery and at the nose of the expanding flux rope accelerates plasma within the flux rope (the core of which formed the filament) into a rotating spire. A component of this untwisting wave also drives part of the flux-rope plasma upwards as the wave propagates²². Rotational and upward velocities within the jet spire approach the local Alfvén speed of around 300 km s^{-1} . Coupled to this are the fast outflows from the flare current sheet, which act to strengthen the rotation and the vertical component of the untwisting wave. This combination of hot jet outflow mixed with cool filament material ejected at a few hundred kilometres per second is exactly what is observed in mini-filament coronal jets^{13,14}.

Figure 2b shows the three-dimensional shape of the jet (see also Supplementary Video 2). The untwisting spire arising from one side of the jet base, opposite the flare loops formed on the other, explains the separation of the spire and compact bright point, respectively, in the observed jets. An example of such an observed mini-filament jet²³ is shown in Extended Data Fig. 2 (see also Supplementary Video 3). The tapered outflow arising from the sharp interface above the mini-filament in Extended Data Fig. 2a and the slight brightening of the right-side loop structure are explained by the positioning of the breakout current sheet and the weak reconnection outflows that we see in our simulation before the onset of the eruptive jet.

Figure 3 illustrates how the main stages of our breakout jet compare with large-scale breakout CMEs. The critical physical difference between the two configurations is the role of expansion. In CMEs, the complete erupting system—the flux rope and overlying field—can expand to many times its original size, as is evident in Fig. 3c, d. This purely ideal expansion, by itself, produces a large energy decrease. The reconnection that is evident in Fig. 3c, d could well be a byproduct of the ideal expansion, rather than the driver of the expansion. In CMEs,

therefore, it is difficult, with either observations or simulations, to separate the effects of the ideal and resistive processes and to determine definitively the mechanism of eruption. In contrast, in coronal jets the background field is strong and drops off negligibly with height over the scale of the jet region, so that the ideal expansion is completely suppressed. The closed-field region in our simulation simply lacks sufficient free energy to push aside the surrounding field and open ideally. We note that in Fig. 3e–h the closed-field region expands only marginally throughout the event. In our simulation, the sharp increase in kinetic energy and the explosive jet are due solely to a rapid increase in reconnection at the breakout current sheet.

Our results yield two far-reaching conclusions. First, the breakout model is universal across multiple scales in the Sun's corona, occurring wherever free magnetic energy builds up at a polarity inversion line. Consequently, our model can explain CME-like eruptions that occur from large¹ to small^{6,7,9} scales, including those associated with jets¹³. The strength of the overlying field and the closed or open nature of this field dictate the appearance of the eruption, with large-scale CMEs and breakout jets at opposite ends of a spectrum that also includes confined flares and failed filament eruptions²⁴ and may even extend to explosive events at still smaller scales, such as chromospheric jets²⁵, spicules²⁶ and Ellerman bombs^{27,28}. Second, the runaway reconnection mechanism of the breakout model, which is inherently a resistive process, is all that is required for explosive eruption. Unlike numerical simulations of large CMEs, in which it is difficult to separate the effects of reconnection from ideal expansion, ideal processes play no substantial part in producing jets. Therefore, our results demonstrate that if coronal jets and CMEs are physically identical in origin, resistive reconnection is the key energy-release mechanism that underlies both phenomena.

Online Content Methods, along with any additional Extended Data display items and Source Data, are available in the online version of the paper; references unique to these sections appear only in the online paper.

Received 15 December 2016; accepted 24 February 2017.

- Webb, D. F. & Howard, T. A. Coronal mass ejections: observations. *Living Rev. Sol. Phys.* **9**, 3 (2012).
- Shibata, K. *et al.* Observations of x-ray jets with the Yohkoh soft x-ray telescope. *Publ. Astron. Soc. Jpn* **44**, L173–L179 (1992).
- Shimojo, M. *et al.* Statistical study of solar x-ray jets observed with the Yohkoh soft x-ray telescope. *Publ. Astron. Soc. Jpn* **48**, 123–136 (1996).
- Savcheva, A. *et al.* A study of polar jet parameters based on Hinode XRT observations. *Publ. Astron. Soc. Jpn* **59**, S771–S778 (2007).
- Shibata, K. Evidence of magnetic reconnection in solar flares and a unified model of flares. *Astrophys. Space Sci.* **264**, 129–144 (1998).
- Innes, D. E., Genetelli, A., Attie, R. & Potts, H. E. Quiet Sun mini-coronal mass ejections activated by supergranular flows. *Astron. Astrophys.* **495**, 319–323 (2009).
- Innes, D. E., McIntosh, S. W. & Pietarila, A. STEREO quadrature observations of coronal dimming at the onset of mini-CMEs. *Astron. Astrophys.* **517**, L7 (2010).
- Raouafi, N.-E., Georgoulis, M. K., Rust, D. M. & Bernasconi, P. N. Micro-sigmoids as progenitors of coronal jets: is eruptive activity self-similar multi-scaled? *Astrophys. J.* **718**, 981–987 (2010).
- Schrijver, C. J. Eruptions from solar ephemeral regions as an extension of the size distribution of coronal mass ejections. *Astrophys. J.* **710**, 1480–1485 (2010).
- Török, T. & Kliem, B. Confined and ejective eruptions of kink-unstable flux ropes. *Astrophys. J.* **630**, L97–L100 (2005).
- Kliem, B. & Török, T. Torus instability. *Phys. Rev. Lett.* **96**, 255002 (2006).
- Yokoyama, T. & Shibata, K. Magnetic reconnection as the origin of X-ray jets and H α surges on the Sun. *Nature* **375**, 42–44 (1995).
- Sterling, A. C., Moore, R. L., Falconer, D. A. & Adams, M. Small-scale filament eruptions as the driver of X-ray jets in solar coronal holes. *Nature* **523**, 437–440 (2015).
- Zhang, Q. M. *et al.* Explosive chromospheric evaporation in a circular-ribbon flare. *Astrophys. J.* **827**, 27 (2016).
- Pariat, E., Antiochos, S. K. & DeVore, C. R. A model for solar polar jets. *Astrophys. J.* **691**, 61–74 (2009).
- Wyper, P. F., DeVore, C. R., Karpen, J. T. & Lynch, B. J. Three-dimensional simulations of tearing and intermittency in coronal jets. *Astrophys. J.* **827**, 4 (2016).
- Nishizuka, N. *et al.* Giant chromospheric anemone jet observed with Hinode and comparison with magnetohydrodynamic simulations: evidence of propagating Alfvén waves and magnetic reconnection. *Astrophys. J.* **683**, L83–L86 (2008).

18. Antiochos, S. K. Helicity condensation as the origin of coronal and solar wind structure. *Astrophys. J.* **772**, 72 (2013).
19. Martin, S. Conditions for the formation and maintenance of filaments. *Sol. Phys.* **182**, 107–137 (1998).
20. Antiochos, S. K., DeVore, C. R. & Klimchuk, J. A. A model for solar coronal mass ejections. *Astrophys. J.* **510**, 485–493 (1999).
21. Karpen, J. T., Antiochos, S. K. & DeVore, C. R. The mechanisms for the onset and explosive eruption of coronal mass ejections and eruptive flares. *Astrophys. J.* **760**, 81 (2012).
22. Shibata, K. & Uchida, Y. Sweeping-magnetic-twist mechanism for the acceleration of jets in the solar atmosphere. *Sol. Phys.* **103**, 299–310 (1986).
23. Moore, R. L., Sterling, A. C. & Falconer, D. A. Magnetic untwisting in solar jets that go into the outer corona in polar coronal holes. *Astrophys. J.* **806**, 11 (2015).
24. DeVore, C. R. & Antiochos, S. K. Homologous confined filament eruptions via magnetic breakout. *Astrophys. J.* **680**, 740–756 (2008).
25. Shibata, K. *et al.* Chromospheric anemone jets as evidence of ubiquitous reconnection. *Science* **318**, 1591–1594 (2007).
26. De Pontieu, B. *et al.* The origins of hot plasma in the solar corona. *Science* **331**, 55–58 (2011).
27. Ellerman, F. Solar hydrogen “bombs”. *Astrophys. J.* **46**, 298–300 (1917).
28. Vissers, G. J. M., van der Voort, L. & Rutten, R. J. Ellerman bombs at high resolution. II. Triggering, visibility, and effect on upper atmosphere. *Astrophys. J.* **774**, 32 (2013).

Supplementary Information is available in the online version of the paper.

Acknowledgements P.F.W. was supported by a Royal Astronomical Society Fellowship at Durham University and previously by a NASA Postdoctoral Program Fellowship at NASA Goddard Space Flight Center. S.K.A. and C.R.D. were supported by NASA ‘Living With a Star’ and Heliophysics Supporting Research grants. The numerical simulations were supported by NASA High-End Computing allocations to C.R.D. on discover at NASA’s Center for Climate Simulation.

Author Contributions P.F.W. designed and performed the numerical simulations, created the graphical outputs, and drafted the manuscript. S.K.A. conceived the investigation, consulted on the simulations, and revised the manuscript. C.R.D. developed the numerical model, assisted in designing the experiments, acquired the computer resources required, and revised the manuscript.

Author Information Reprints and permissions information is available at www.nature.com/reprints. The authors declare no competing financial interests. Readers are welcome to comment on the online version of the paper. Publisher’s note: Springer Nature remains neutral with regard to jurisdictional claims in published maps and institutional affiliations. Correspondence and requests for materials should be addressed to P.F.W. (peter.f.wyper@durham.ac.uk).

Reviewer Information *Nature* thanks K. Shibata and the other anonymous reviewer(s) for their contribution to the peer review of this work.

METHODS

Numerical experiment details. The simulation was conducted using the Adaptively Refined Magnetohydrodynamics Solver (ARMS), to solve the ideal magnetohydrodynamic equations on an adaptively refined grid. Reconnection occurs through numerical diffusion, and an adiabatic energy equation is used in the manner of our previous calculations^{15,16}. The energy equation used in our simulation captures heating/cooling from compression/expansion. However, heating from ohmic and viscous dissipation, cooling from radiative losses, and energy transfer by thermal conduction are not captured. The dynamics are dominated by the magnetic field because the thermal pressure and plasma beta (the ratio of thermal to magnetic pressure) are low, so we expect that their inclusion would produce local differences in plasma temperature and density, but that the plasma dynamics would not change very much. We also expect that the general evolution of magnetic and kinetic energies would be largely unchanged, although the precise values would certainly vary somewhat owing to the competing effects of the additional sources or sinks in energy.

The initial potential magnetic field of the simulation consists of a uniform background field of -2 G inclined 22° to the vertical, superimposed upon a set of 16 (8 positive and 8 negative) sub-photospheric dipoles aligned vertically and arranged to yield strong positive and negative polarity patches on the photosphere, typical of emerged bipolar regions. The combined strengths of the various dipoles and background field give peak vertical field strengths in the positive and negative patches of 34 G . The atmosphere consists of uniform plasma at a temperature of 1.2 MK and a density of $4 \times 10^{-16}\text{ g cm}^{-3}$. In the corona, the plasma beta is well below unity, so the dynamics are dominated by magnetic forces. In our simulation, the beta is 2×10^{-1} in the background field and drops to 9×10^{-4} in the centre of the strong-field patch of the bipole on the photosphere (situated at $x=0$). The driving on the photosphere is the same as used in our previous calculations^{15,16} and follows the contours of the vertical field component at the photosphere. This maintains the initial potential field as the lowest-energy state throughout the simulation, so any change in the magnetic energy represents stored free energy. The peak driving speed is 30 km s^{-1} , which is faster than typically inferred flow speeds on the solar surface²⁹ but still much slower than the local Alfvén ($4,850\text{ km s}^{-1}$) and sound (130 km s^{-1}) speeds. Thus, the system evolves quasi-statically until the internal dynamics become fast. The driving is ramped up, held constant for

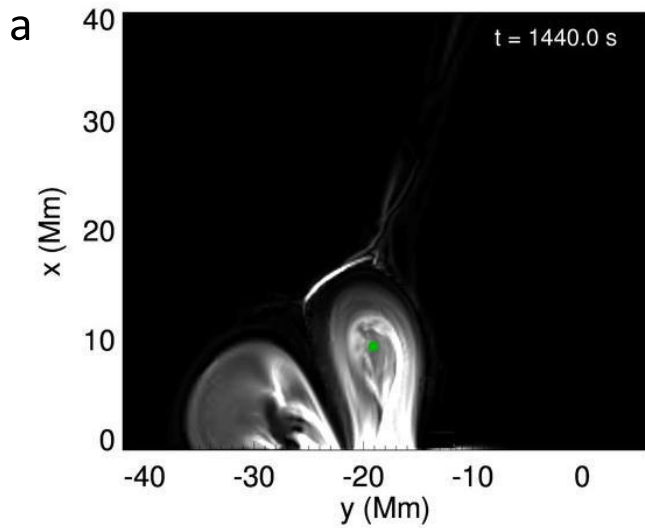
a time, and then is ramped back down to zero over a period of 20 min (Fig. 4). There is a small overlap of the driving interval with the onset of the breakout reconnection; however, the driving has long ceased when the flux rope opens and the jet is launched, at time $t = 28\text{ min}$. The numerical domain has dimensions [600 Mm, 600 Mm, 200 Mm], large enough that the jet does not reach the boundary before the simulation is halted. The numerical grid adapts according to criteria²¹ that refine the grid in regions of medium- to high-strength current and de-refine otherwise (Extended Data Fig. 3). We used six levels of refinement in this simulation. The resolution necessary for an equivalent fixed-grid calculation would be $4,608 \times 4,608 \times 1,536$, making this by far the highest-resolution three-dimensional calculation of its type to date.

Flux-rope rise-speed calculation. The rise speed of the flux rope during the breakout-reconnection phase was calculated by inspecting contour plots of current density in the plane ($z=0$) that the flux rope crosses perpendicularly. The centre of the flux rope was estimated by eye as the centre of the circular current region that forms above the polarity inversion line of the bipole (Extended Data Fig. 1a). For each frame until the flux rope opened, this procedure was repeated; the rise speed was then calculated from the rate of change of the centre position (Extended Data Fig. 1b). We stopped tracking the flux rope shortly before its reconnection with the open field. After this time the axis of the rope aligns with the ambient field and the speed of the filament plasma cannot be estimated with this method. Extended Data Fig. 1a shows one frame of Supplementary Video 4, depicting the movement of the tracked position with time.

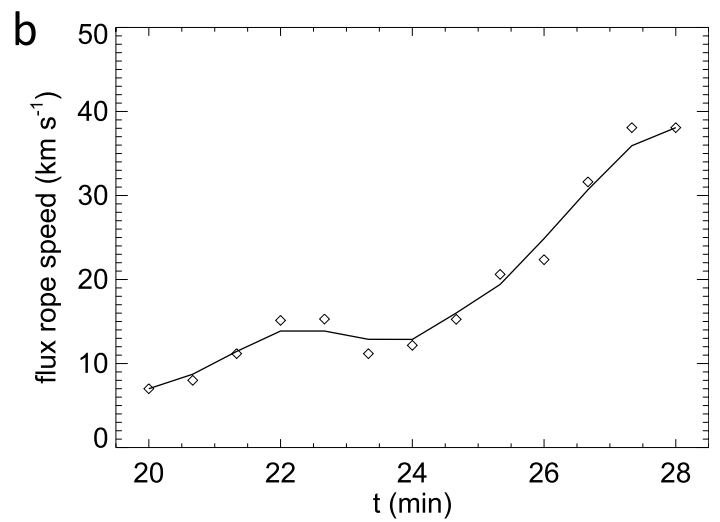
Code availability. We have opted not to make ARMS available owing to its complexity, which demands expert assistance to set up, run and analyse simulations, and because it is continually being improved and extended, which requires frequent software updates. Interested parties are invited to contact the authors for more detailed information.

Data availability. The three-dimensional simulation data generated and analysed for this paper occupy approximately 200 GB. Interested parties are invited to contact the authors to make arrangements for the transfer of those data. The one-dimensional reduced data in Fig. 4 and ED Fig. 1 are provided as Source Data.

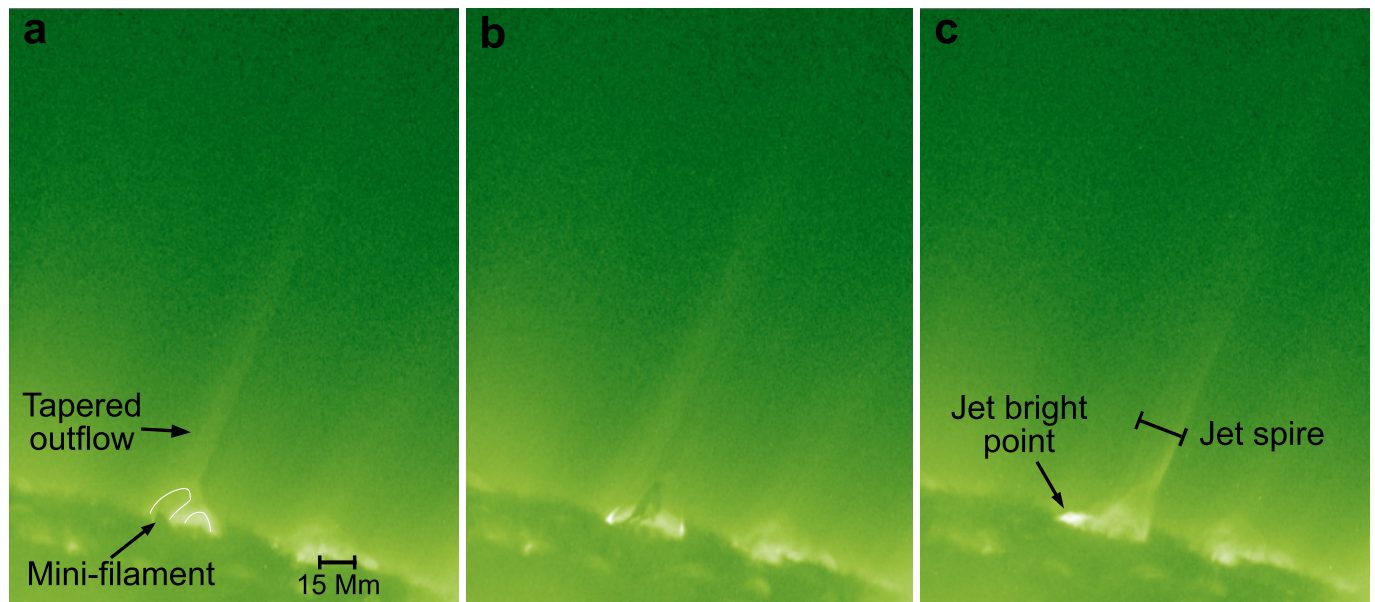
29. Brandt, P. N. *et al.* Vortex flow in the solar photosphere. *Nature* **335**, 238–240 (1988).



Extended Data Figure 1 | Estimate of the speed of the flux rope during the slow-rise phase. a, Current density (saturated at $6 \times 10^{-3} \text{ A m}^{-2}$) in the $z = 0$ plane; x and y are the vertical and horizontal Cartesian coordinates. The green dot shows the position near the centre of the

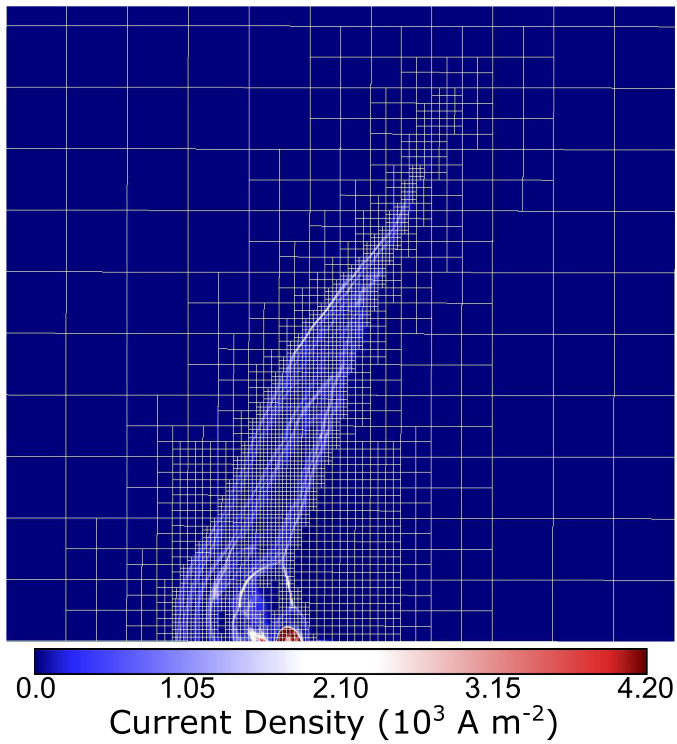


flux rope that is tracked in time. **b,** Inferred speed of the flux rope axis (diamond symbols); the solid line shows these data after applying a two-point boxcar smoothing.



Extended Data Figure 2 | Example of a mini-filament jet. A large coronal jet produced in conjunction with the eruption of a mini-filament²³, as seen by the Solar Dynamics Observatory's Atmospheric Imaging Assembly in Fe XII at wavelength $\lambda = 193 \text{ \AA}$. **a-c**, Images prior to the jet (**a**), during the

jet (**b**) and after the jet (**c**). The inferred coronal loop structure is depicted in white in **a**. We are grateful to R. L. Moore for providing the unpublished video from which these images were extracted.



Extended Data Figure 3 | The block-adapted mesh during the jet, in the $z=0$ plane at $t=32 \text{ min } 40 \text{ s}$. Each box corresponds to a block of $8 \times 8 \times 8$ cells. Grid parameters are chosen to refine in regions of medium- to high-current density, shown as regions of white and red. The grid increases in size by a factor of four during the simulation, and the minimum resolution is 104 km.